Supporting Information

Polycrystallinity of Lithographically Fabricated Plasmonic Nanostructures Dominates Their Acoustic Vibrational Damping

Chongyue Yi[1, ‡], Man-Nung Su[1, ‡], Pratiksha D. Dongare[2,3], Debadi Chakraborty[4], Yi-Yu Cai[1], David M. Marolf[1], Rachael N. Kress[1], Behnaz Ostovar[1], Lawrence J. Tauzin[1], Fangfang Wen[1], Wei-Shun Chang[1], Matthew R. Jones[1], John E. Sader[4*], Naomi J. Halas[1,3,5,6*], and Stephan Link[1,3,6*]*

1. Department of Chemistry, Rice University, Houston, Texas, 77005, USA.
2. Applied Physics Graduate Program, Rice University, Houston, TX 77005, USA.
3. Department of Electrical and Computer Engineering, Rice University, Houston, Texas 77005, USA.
4. ARC Centre of Excellence in Exciton Science, School of Mathematics and Statistics, The University of Melbourne, Parkville, VIC 3010, Australia
5. Department of Physics and Astronomy, Rice University, Houston, Texas, 77005, USA.
6. Laboratory for Nanophotonics, Rice University, Houston, Texas, 77005, USA.

Corresponding authors: mrj@rice,edu, jsader@unimelb.edu.au, halas@rice.edu, slink@rice.edu

‡These authors contributed equally.

Table of Contents

1. Methods and data analysis

1a. Sample preparation

Electron-beam lithography. Individual Au nanostructures were fabricated on a glass substrate using electron-beam lithography. The substrates were sonicated in acetone for 5 min, rinsed with isopropyl alcohol (IPA), cleaned in an oxygen plasma for 5 min and spin-coated with a layer of polymethyl methacrylate resist (PMMA 950 A2, MicroChem) and Espacer 300Z (Showa Denko). Electron-beam patterning of the resist was performed using a FEI QUANTA 650 SEM with a voltage of 30 K and a beam current of 40 pA. The resist was then developed in a 1:3 methyl isobutyl ketone (MIBK): IPA solution. Titanium adhesion and gold layers were deposited on the substrates by electron-beam evaporation. The thickness of the deposited metals was monitored by a quartz crystal microbalance and further confirmed by AFM measurements.[1] The structures were treated with a standard lift-off process via incubation in N-methyl-2-pyrrolidone at 65 °C for 2 h.

Gold nanorod synthesis. Au nanorods were synthesized by using a seeded growth method described in previous work.[2] Briefly, the seeds were prepared by mixing of 5 mL 0.5 mM $HAuCl_4$ and 5 mL 0.2 M cetyl trimethylammonium bromide (CTAB) with 1 mL 0.006 M $NaBH_4$. The seed solution was vigorously stirred (1200 rpm) for 2 min, and aged 30 mins before use. The growth solution was prepared by dissolving 7 g CTAB and 1.234 g sodium oleate with 240 mL hot water (80 °C). After the growth solution was cooled down to 30 °C, the seed solution was injected. This mixture was kept at 30 °C for 15 min. Then 240 mL 1 mM $HAuCl_4$ was added and was stirred at 700 rpm for 90 min. The final step was to inject 1.25 mL 0.064 M ascorbic acid (stirring for 30 s), and 0.4 mL seed solution (stirring for 30 s) into the growth solution. The seeds were allowed to grow at 30 °C for 12 h without stirring. The product, Au nanorods, was concentrated using centrifugation at 8000 rpm for 30 min.

Gold nanodisk synthesis. Colloidal Au nanodisks were synthesized following literature methods.[3] Briefly, triangular Au nanoprisms (~ 180 nm edge length) were synthesized following a seed-mediated growth process and separated from spherical nanoparticle impurities via a depletion-force mediated selective crystallization. The purified triangular prisms (0.5 optical density at λ = 1270 nm) in 50 mM CTAB were then brought to 12 mM $HAuCl_4$. The ensuing conproportionation reaction selectively oxidizes the Au-(0) at the nanoprism tips and is self-limiting. The resulting particles, therefore, are circular disks of the same thickness as the original triangular prisms (7.5 nm) with a diameter of 97 nm.

1b. Annealing procedure of lithographically prepared Au nanodisks

Gradual annealing was achieved by focusing the laser on a nanodisk of interest and gradually increasing the power incrementally over time. 178 nm Au nanodisks were used for the annealing process. The power of a 488 nm diode laser (Coherent OBIS) was set to 3 mW and the laser was focused on an individual structure for 1 hr. After 1 hr., the laser power was increased to 4 mW for an additional hr. The laser power was next adjusted to 6 mW for a final hr.

1c. Dark-field scattering spectroscopy

Scattering spectra of individual nanostructures were measured using a dark-field spectroscopy setup based on an inverted microscope (Zeiss Axio Observer m1). White light was focused onto the sample using an oil-immersed condenser (Zeiss, N.A. = 1.4). For the nanodisks having a broad spectral response, the scattered signals were collected

by a 74 × reflective objective (Beck Optronic Solutions, N. A. = 0.65). For the nanorods which exhibited a narrower spectral response, the scattering light was collected by a 50 × objective (Zeiss, N. A. = 0.8). In both cases, the scattered light was directed into a spectrograph (Princeton Instruments Acton 2156i) towards a charge-coupled device camera (Princeton Instruments Pixis 400BR). A spectrum was obtained by dividing the collected signal by the white light spectrum after subtracting background noise.

1d. Single-particle transient extinction spectroscopy

A diode-pumped laser (Coherent Verdi) was used to pump a Ti-Sapphire oscillator (KMLab Griffin) to generate a 810 nm beam with a pulse duration of ~80 fs. The 405 nm pump beam was generated by frequency-doubling part of the 810 nm fundamental beam in a beta barium borate crystal (Altos BBO-1004H). The other part of the 810 nm femtosecond beam was selected as probe. The probe beam passed through an optical delay line (Newport UTS150CC), and the intensity of the pump beam was modulated by an acousto-optic modulator (IntraAction AOM-402AF1) with a frequency of 720 kHz. The pump and probe beams were collinearly overlapped by a dichroic mirror before being focused onto the sample by the same objective (Zeiss, N. A.=1.4). The pump (405 nm) and probe (810 nm) powers were 150 and 50 μW, respectively, unless mentioned specifically. The powers of pump and probe focused on a single structure were 9.27×10^4 W/cm^2 and 2.26×10^4 W/cm^2. The beam polarizations were manipulated with half wave plates positioned before the dichroic mirror that combined pump and probe beams. A parallel configuration of linearly polarized pump and probe beams was employed. The diameters of both pump and probe beams were tuned large enough to ensure that the entire nanostructure was excited and probed. The pump and probe beams were collected by a second objective (Zeiss, N. A.=0.6) in a transmission geometry and passed through a 450 nm long-pass filter so that only the probe beam was detected by a photodiode. The signal was fed into a lock-in amplifier and connected to a data acquisition board (National Instruments). Transient extinction images, used to locate individual nanodisks, were obtained with pump and probe beams overlapped temporarily by scanning the sample through the focused laser beams using a piezo scanning stage (Physik Intrumente P-517.3CL). Time transients were acquired by moving the optical delay line and repeated at least two times to ensure the reproducibility of each measurement and photostability of the sample.

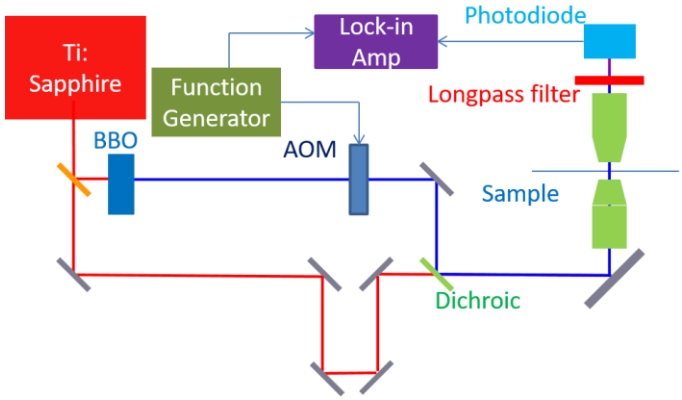

Figure S1. Experimental setup of the time-resolved transient extinction microscope. BBO: beta barium borate crystal; AOM: acousto-optic modulator; Lock-in Amp: lock-in amplifier. The pump wavelength was fixed at 405 nm. The probe wavelength was set at 810 nm. The pump laser power was 150 μW, while the probe laser power was 50 μW.

1e. Fitting procedure

The transient differential transmission $\Delta T/T$ can be described by the following equation:

$$\frac{\Delta T}{T} = g(t)\left(a_1\, exp\left(-{}^{t}/_{t_1}\right) + a_2\, exp\left(-{}^{t}/_{t_2}\right)\right) + b\, exp\left(-{}^{t}/_{\tau}\right) sin(2\pi\nu t + \varphi) \quad \text{(S1)}$$

where T is the transmission, $g(t)$ is a Gaussian instrument response function, a_1 and a_2 are amplitude coefficients, t_1 is the electron-phonon coupling time, t_2 is the decay time for thermal coupling to the environment, τ is the damping time of the vibrational mode, ν is the vibrational frequency, b is the vibrational amplitude, and φ is a phase factor. All the error bars reported for transient extinction data correspond to the standard deviation from several measurements performed on at least 7 different nanostructures with the same size and geometry. Note that the new transient transmission data collected in this work was measured to longer delay times compared to our previous work. This approach resulted in both more accurate values obtained from the fits and slightly longer damping time. As a consequence, the average Q factor for gold nanodisks reported here is larger, but nevertheless both old and new measurements agree within the error bars.[1, 4, 5] Our new results here are furthermore more consistent with the literature.[6-10]

1f. FEM modeling

Three-dimensional gold nanostructures were modeled in the commercial finite element software COMSOL Multiphysics using its eigenfrequency solver for the Navier's equation. In order to consider the interaction between gold nanostructures without and with a 2 nm Ti adhesion layer and the glass substrate, a free surface model was considered. In one case, the bottom surface of the nanostructure was allowed to freely expand and contract just like the top surface, simulating a non-interacting substrate. To demonstrate the influence of the substrate on the Q factor, we used the frequency response solver of COMSOL Multiphysics. To truncate the thickness of the thicker glass layer, a perfectly matched layer (PML) on the bottom of the glass substrate was used to absorb propagating acoustic waves. The reported results are independent of mesh size to within 0.1%.

2. Scattering spectra of nanodisks plotted as a function of photon energy

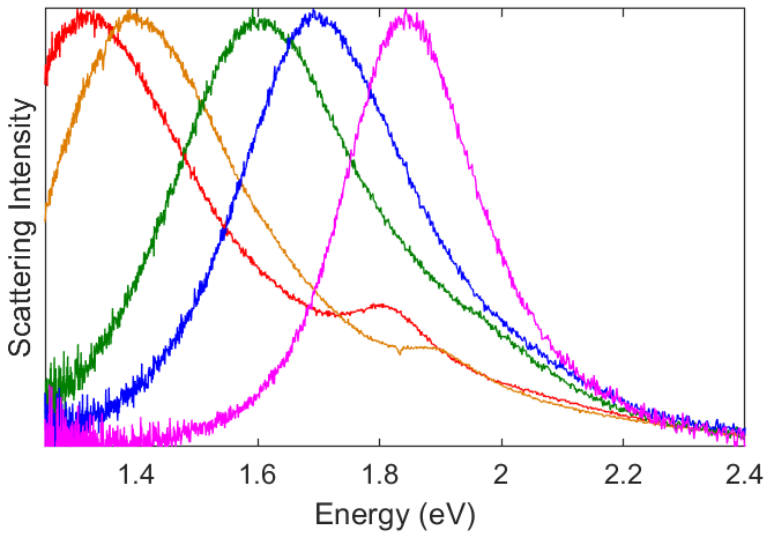

Figure S2. Experimental single-particle scattering spectra of Au nanodisks. The scattering intensities are plotted as a function of photon energy. The diameters of the nanodisks varied from 240 nm (red), 205 nm (orange), 178 nm (green), 160 nm (blue), to 120 nm (magenta). The linewidths (full width at half maximum) of these spectra are 0.42, 0.39, 0.39, 0.34, and 0.26 eV, respectively. The linewidths were determined by fitting the dipole resonance to a Lorentzian function. As the diameter decreases from 240 nm to 120 nm, the plasmon resonance becomes narrower.

3. Size-dependent acoustic vibrations of Au nanodisks

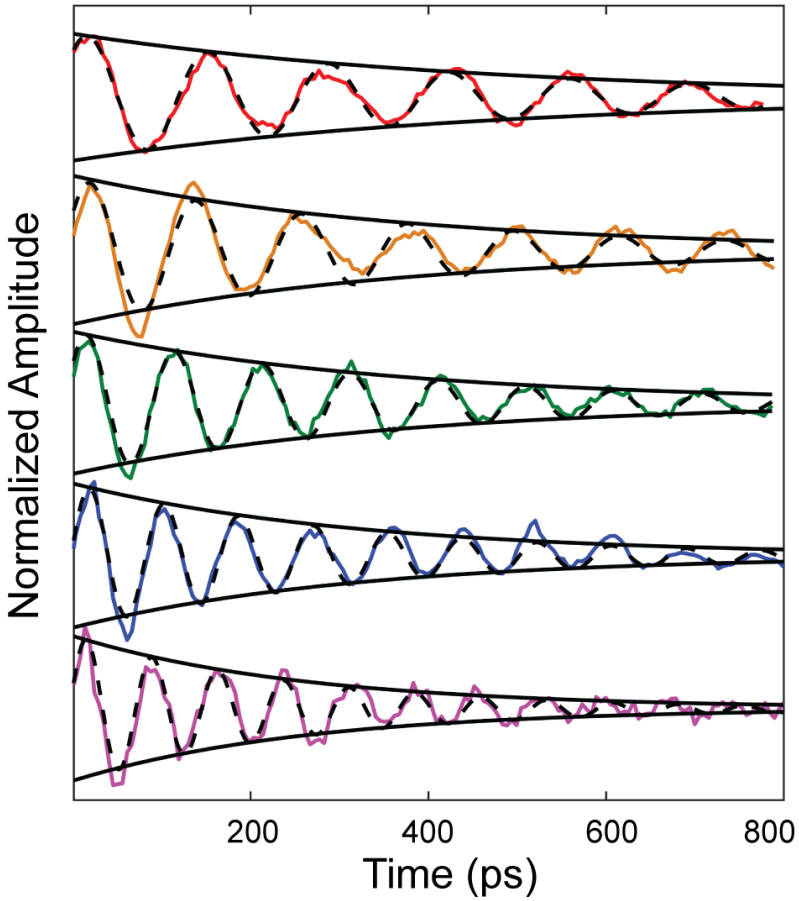

Figure S3. Acoustic vibrations of individual Au nanodisks with different sizes. The diameters of nanodisks varied from 120 nm (magenta), 160 nm (blue), 178 nm (green), 205 nm (orange), and 240 nm (red). The time-dependent amplitude traces were fitted with a damped sine wave function (dashed black line). The exponential decay term extraced from the damped sine wave function is plotted as solid black lines. The oscillation amplitude damped faster in smaller nanodisk. Data are normalized and offset for better comparison.

4. Thickness dependent acoustic vibrations of Au nanodisks

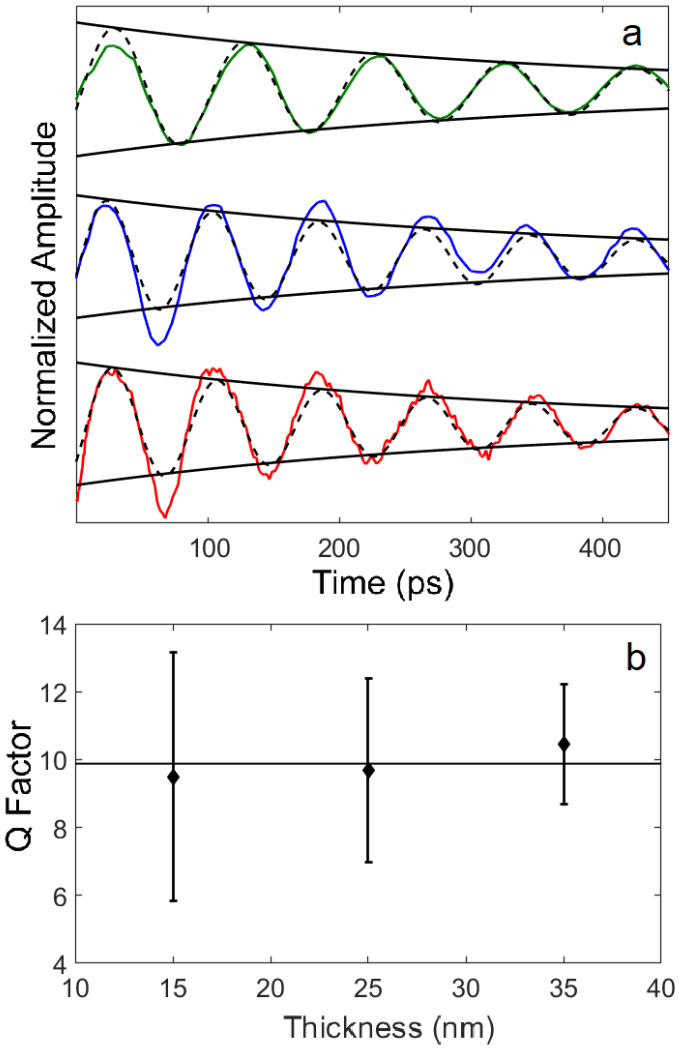

Figure S4. Disk thickness dependent acoustic vibrations of Au nanodisks. (a) Transient transmissions of Au nanodisks with different thicknesses (red: 15 nm, blue: 25 nm, and green: 35 nm). The diameter of the nanodisks was constant at 178 nm. The black dashed lines represent the fits based on a damped sine wave. The exponential decay term extracted from the fit is also plotted as black solid lines. Data are normalized and offset for better comparison. (b) Disk thickness dependence of the Q factor, which is not dependent on the Au nanodisk thickness. The average Q factor is shown as the black line.

5. FEM simulation of Q factors of Au nanodisks

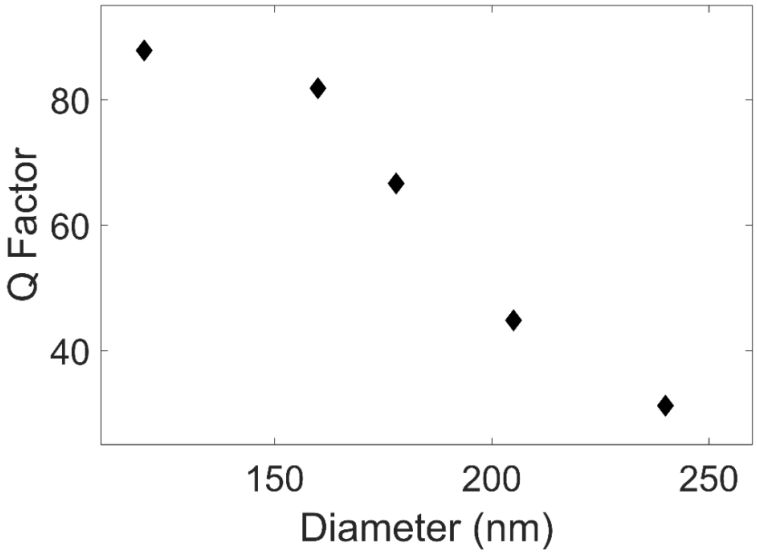

Figure S5. Simulation of Q factors for different Au nanodisks. In these FEM simulations, Au nanodisks with a 2 nm Ti adhesion layer were attached on top of a glass substrate. The Young's modulus of the coupling layer was 70 GPa. As the disk diameter and hence contact area between metal and substrate increases, the Q factor decreases.

6. Substrate and Ti layer *Q* factor dependence of Au nanodisks

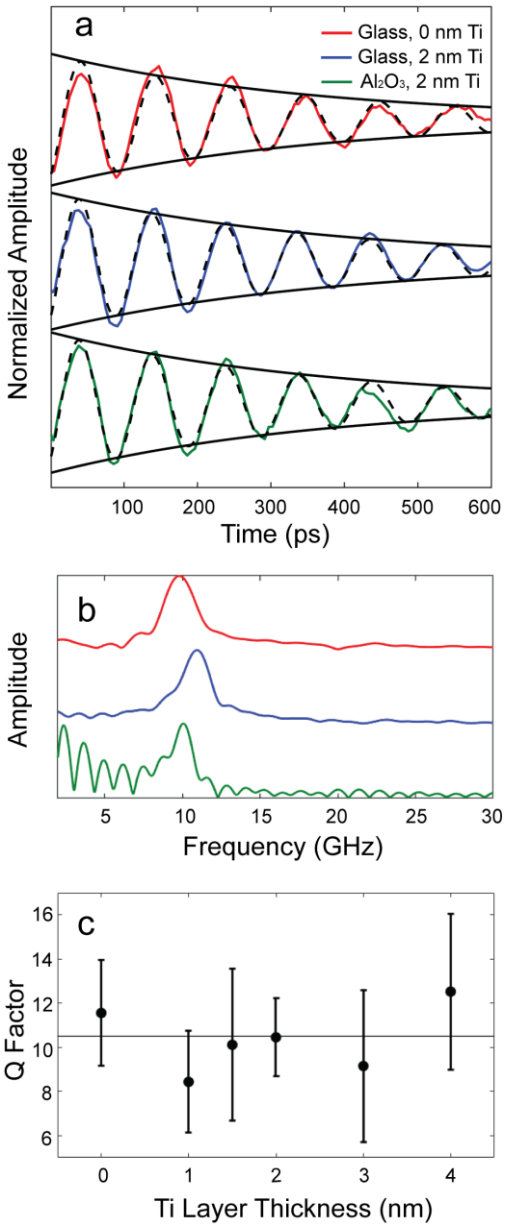

Figure S6. Substrate dependent acoustic vibrations of Au nanodisks. (a) Transient transmissions of Au nanodisks with different substrates and adhesion layers. The diameter of the nanodisks was 178 nm. The black line represents the fit based on a damped sine wave. The exponential decay term extracted from the fit is also plotted as a black solid line. Data are normalized and offset for better comparison. (b) Fourier transform analysis of the time-dependent vibrational amplitudes in Figure S6a, showing the dependence of the acoustic vibration frequency on the adhesion strength to the substrate. (c) Ti adhesion layer thickness dependence of the *Q* factor. The *Q* factor averaged over all Ti adhesion layer thicknesses is shown as the black line. Data from Yi *et al*. was used in panels S6a and S6b, while data from Chang *et al*. was used in panel S6c.[1, 5] While we hypothesized in Chang *et al.* that the variation in damping times and hence *Q* factors is caused by the nature of the adhesion Ti-Au-glass interfaces, the more comprehensive measurements and analysis presented in this work let us conclude that mainly the polycrystallinity of the Au nanostructures is the dominant factor.

7. Solvent dependence of acoustic vibration damping

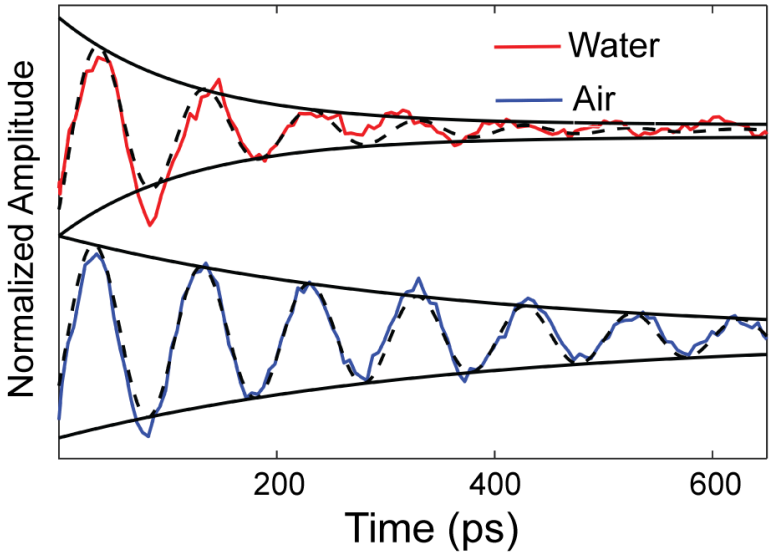

Figure S7. Acoustic vibration of a 178 nm Au nanodisk immersed in different environments; blue: air; red: water. The time-dependent amplitude traces were fitted with a damped sine wave function (dashed black line). These results show that the breathing mode damping time is strongly dependent on the environement. Data are normalized and offset for better comparison.

8. Characterization of Au nanorods with different lengths

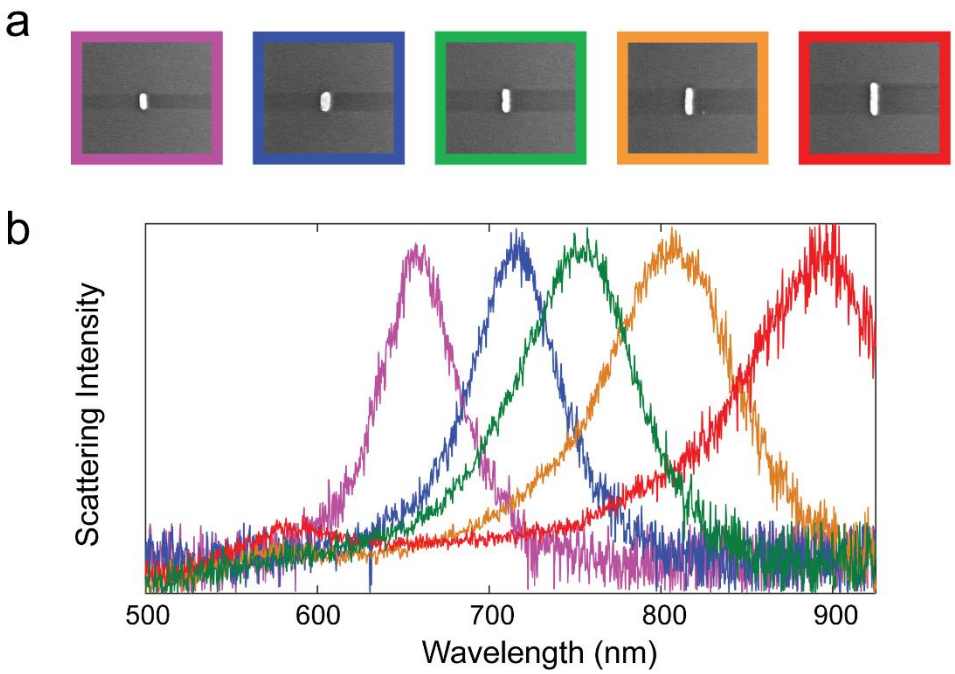

Figure S8. Shape dependent optical properties of Au nanorods. (a) SEM images of individual Au nanorods with different lengths, varied from 80 nm (magenta), 100 nm (blue), 120 nm (green), 140 nm (orange), to 160 nm (red). The width and thickness of the nanorods were fixed at 35 nm. The thickness of the Ti adhesion layer was 2 nm. The size of each SEM image is 640 × 550 nm. (b) Experimental single-particle scattering spectra of Au nanorods with different lengths. As the length increases, the plasmon resonance maximum shifts to longer wavelengths due to an increase of aspect ratio.

9. Length dependent acoustic vibrations of Au nanorods

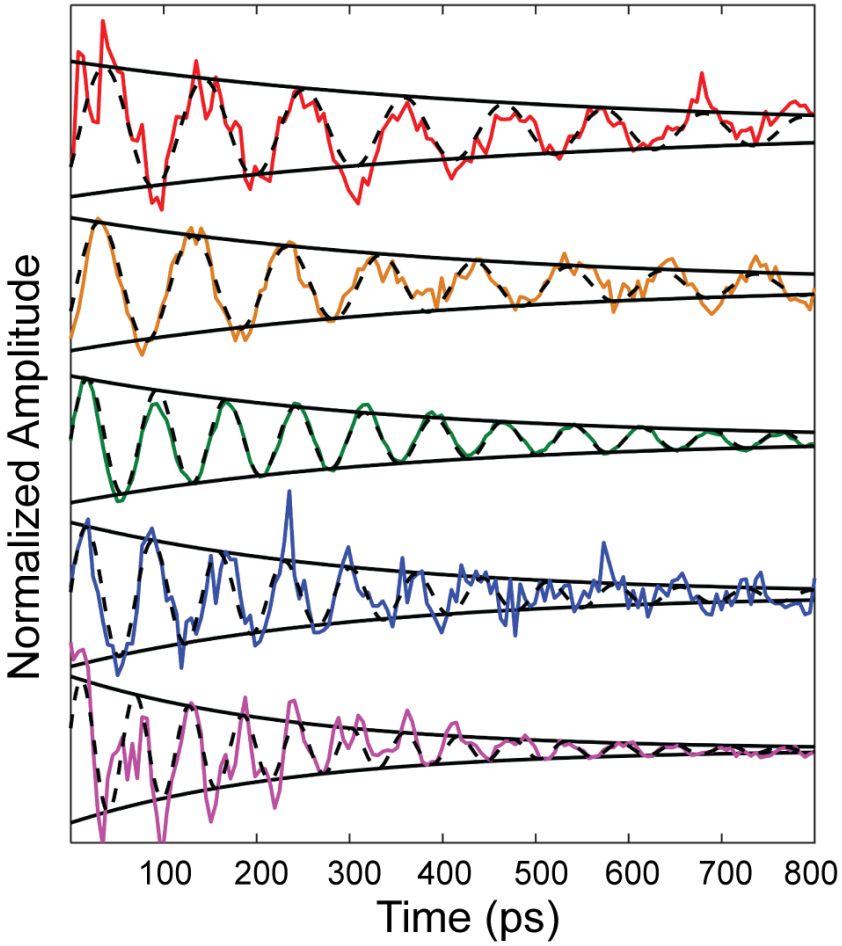

Figure S9. Acoustic vibrations of individual Au nanorods with different lengths. The length of the nanorods varied from 80 nm (magenta), 100 nm (blue), 120 nm (green), 140 nm (orange), to 160 nm (red). The width and thickness of the nanorods were fixed at 35 nm. The time-dependent amplitude traces were fitted with a damped sine wave function (dashed black line). The exponential decay term extraced from the damped sine wave is plotted as the solid black lines. The oscillation amplitude damps faster in smaller nanorods. Data are normalized and offset for better comparison. To maintain the same condition as used for Au nanodisks, the excitation wavelength was set at 405 nm and the probe wavelength was 810 nm.

10. Length dependent vibrational properties of Au nanorods

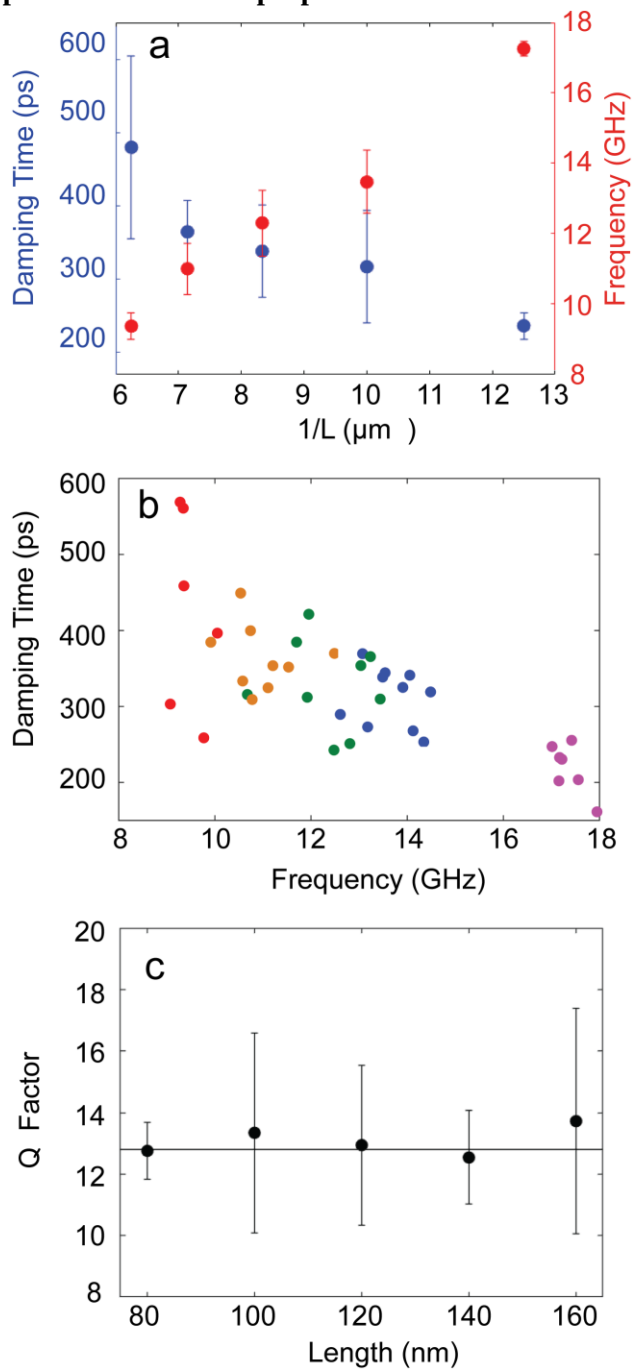

Figure S10. Shape dependent mechanical properties of Au nanorods. (a) Acoustic frequencies (red) and damping times (blue) as a function of inverse Au nanorod length. (b) Scatter plot of the frequencies versus damping times of the extensional mode for single Au nanorods with different lengths, varied from 80 nm (magenta), 100 nm (blue), 120 nm (green), 140 nm (orange), to 160 nm (red). (c) Length dependent Q factors of Au nanorods. The average Q factor (12.6) of all nanorods is shown as the black line. The acoustic vibration damping is not dependent on the shape of nanorods.

11. Characterization of Au nanorods with different widths

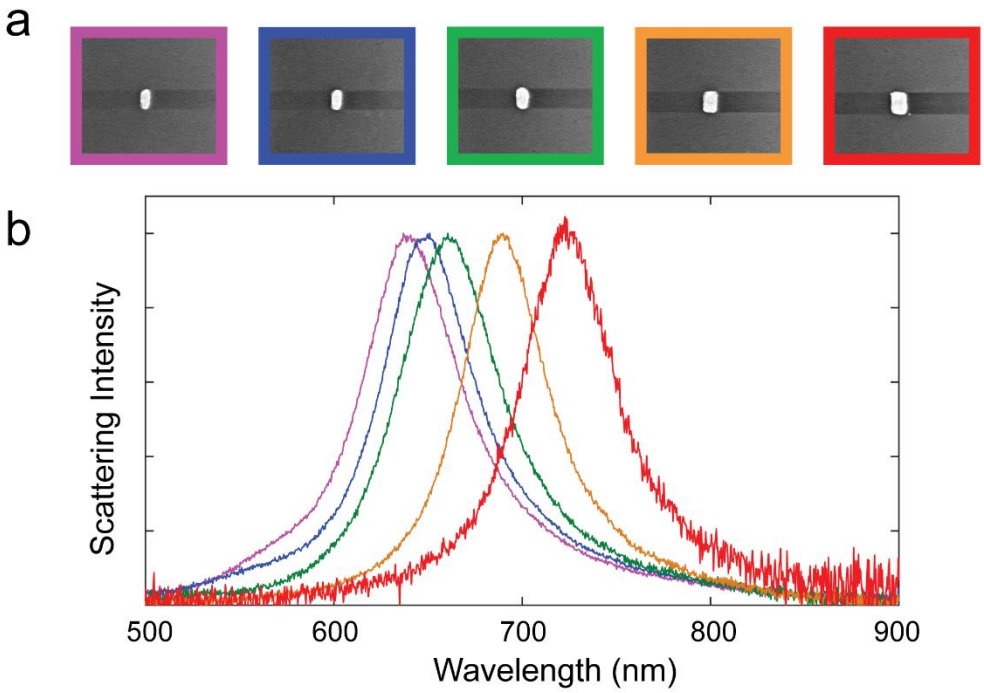

Figure S11. Width dependent optical properties of Au nanorods. (a) SEM images of individual Au nanorods with different widths, varied from 75 (magenta), 65 nm (blue), 55 nm (green), 45 nm (orange), and 35 nm (red). The length of the nanorods was fixed at 100 nm. The thickness of the nanorods was fixed at 35 nm. The thickness of the Ti adhesion layer was 2 nm. The size of each SEM image is 640 × 550 nm. (b) Experimental single-particle scattering spectra of Au nanorods with different widths. As the width decreases, the plasmon resonance maximum shifts to longer wavelengths due to an increase in aspect ratio.

12. Width dependence of acoustic vibration damping for Au nanorods

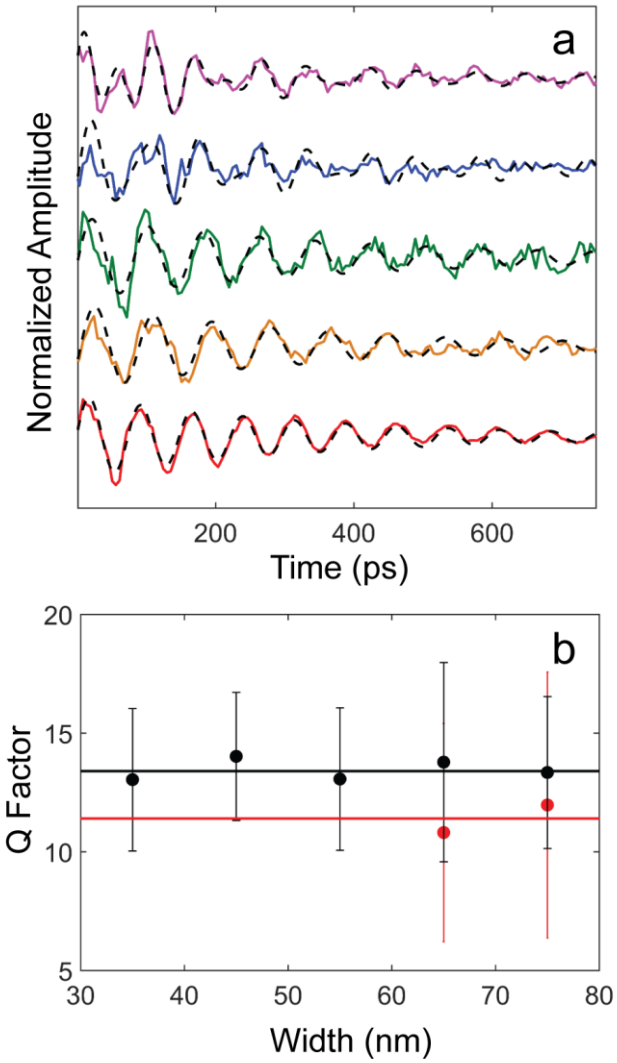

Figure S12. (a) Acoustic vibrations of individual Au nanorods with different widths. The width of the nanorods varied from 75 nm (magenta), 65 nm (blue), 55 nm (green), 45 nm (orange), to 35 nm (red). The length was fixed at 100 nm, while the thickness was constant at 35 nm. The time-dependent amplitude traces were fitted with a damped sine wave function (dashed black line). Data are normalized and offset for better comparison. (b) Width dependent Q factor of Au nanorods. The black dots represent the Q factor of the extensional mode. For Au nanorods with widths of 65 and 75 nm, we also detected the radial breathing mode, and the Q factors are plotted as red dots. The average Q factor (13.4) of extensional mode is shown as the black line. The average Q factor (11.4) of breathing mode is shown as the red line. As the width increased from 35 nm to 75 nm, the Q factor did not change. Similar Q factors for both extensional and breathing modes imply that the surface area does not matter, and hence surface defects do not play a role in acoustic mode damping.

13. Characterization of chemically prepared Au nanorods

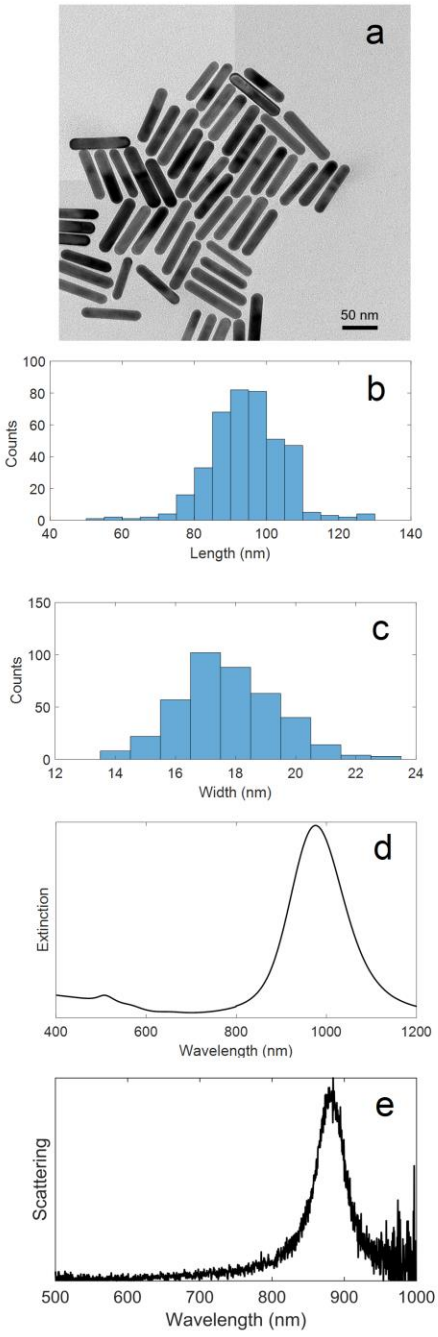

Figure S13. (a) TEM image of chemically prepared Au nanorods. The average length and width were 95 ± 10 and 18 ± 2 nm. (b) Histogram of nanorod length. (c) Histogram of nanorod width. (d) Extinction spectrum of Au nanorods dispersed in water. (e) Single-particle scattering spectrum of an Au nanorod on top of a glass substrate in air.

14. Ligand dependence of acoustic vibrations in chemically prepared Au nanorods

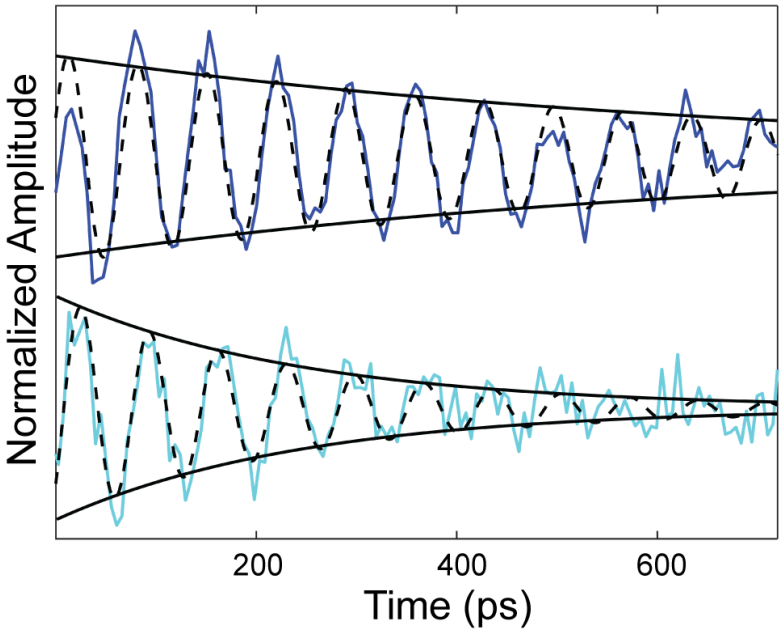

Figure S14. Acoustic vibrations of a single Au nanorod prepared via chemical synthesis before (sky blue) and after (blue) removing the CTAB ligands and residual water. The dimensions of the chemically prepared nanorods were 18 × 95 nm. The dashed black line represents the fit based on a damped sine wave function. The exponential decay term extracted from the damped sine wave is plotted as the solid black lines. The surface ligand, CTAB, was successfully removed by ozone treatment. The larger damping rate of the sample with CTAB surface ligands is attributed to the lubrication effect.[5] Before removal of CTAB, the acoustic vibration frequency was 14.0 ± 0.8 GHz with a damping time of 300 ± 70 ps and Q factor of 13.1 ± 3.2. After removal of CTAB, the acoustic vibration frequency was 14.5 ± 0.8 GHz with a damping time of 501 ± 62 ps and Q factor of 22.0 ± 2.4. Data are normalized and offset for better comparison.

15. Characterization of chemically prepared Au nanodisks

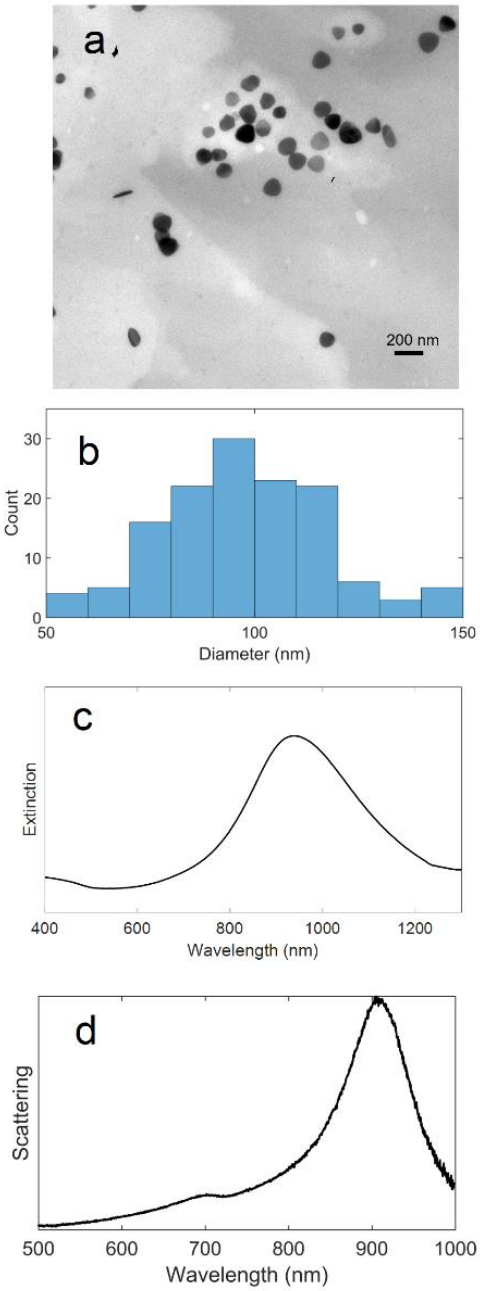

Figure S15. (a) TEM image of chemically prepared Au nanodisks. The average diameter was 92 ± 18 nm. The thickness was approximately 7.5 nm.[3] (b) Histogram of nanodisk diameter. (c) Extinction spectrum of Au nanodisks dispersed in water. (d) Single-particle scattering spectrum of an Au nanodisk on top of a glass substrate in air.

16. Acoustic vibration of an annealed Au nanodisk

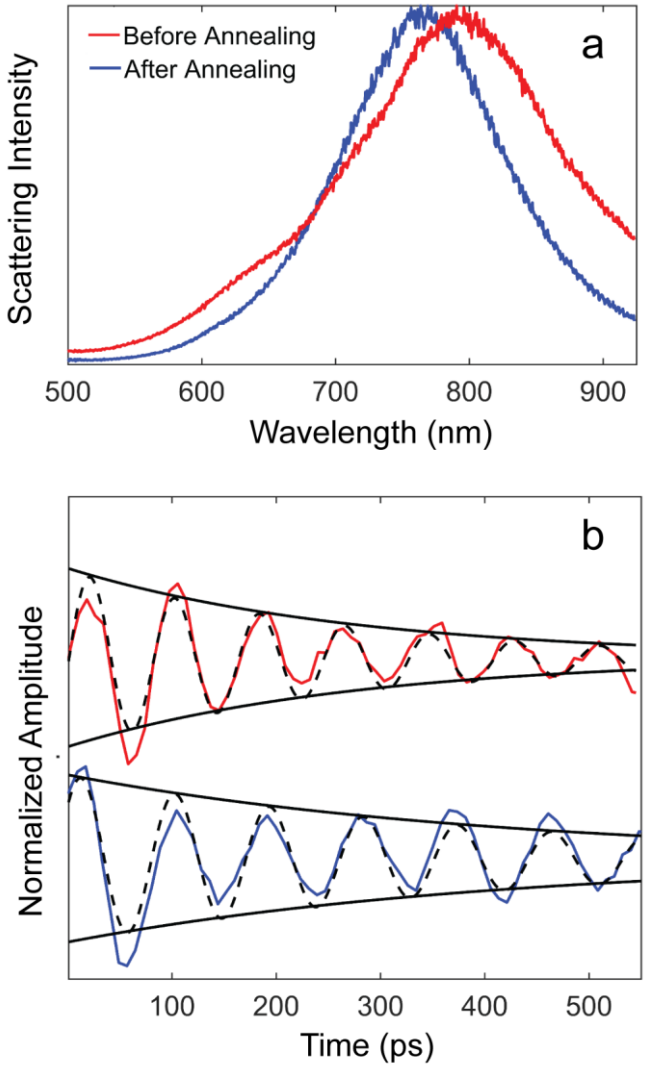

Figure S16. (a) Scattering spectra of a lithographically fabricated Au nanodisk before (red) and after (blue) laser annealing. The diameter of the nanodisk was 178 nm. The thickness was 35 nm. The blue shift and narrowing of the scattering spectrum suggests the successful removal of internal crystal defects. (b) Acoustic vibrations of a nanodisk before and after annealing. The dashed black lines represent the fit based on a damped sine wave function. The exponential decay term extracted from the fit is plotted as the solid black lines. After annealing and improving the crystal quality, the Q factor of the Au nanodisk increased from 11.0 ± 1.8 to 14.8 ± 0.8. Data are normalized and offset for better comparison.

17. Table S1. Size distribution of the nanodisks prepared by e-beam lithography

Designed diameter (nm)	120	160	178	205	240
Measured diameter (nm)	119.2	158.3	179.2	206.8	238.3
Standard deviation (%)	0.89	1.90	0.81	1.99	1.62

18. Table S2. Acoustic vibrations extracted from Figures S6 and S7

Substrate	Environment	Frequency (GHz)	Damping Time (ps)	Q Factor
Glass	Water	10.8 ± 0.6	159 ± 37	5.4 ± 1.3
Glass	Air	10.7 ± 0.8	330 ± 73	10.1 ± 1.8
Al_2O_3	Air	10.9 ± 0.4	386 ± 118	13.2 ± 4.1

19. Table S3. Size distribution of the nanorods prepared by e-beam lithography

Designed length (nm)	80	100	120	140	160	100	100	100	100
Designed width (nm)	35	35	35	35	35	45	55	65	75
Measured length (nm)	80.7	97.9	121	139	156	99.0	103	102	104
Standard deviation of length (%)	2.4	1.8	1.5	3.1	2.0	4.1	4.5	3.6	2.5
Measured width (nm)	34.7	38.8	38.0	36.7	35.2	48.1	57.1	67.5	75.7
Standard deviation of width (%)	8.1	5.2	4.4	7.0	6.6	4.7	3.0	2.8	3.4

References

1. Chang, W. -S.; Wen, F.; Chakraborty, D.; Su, M. -N.; Zhang, Y.; Shuang, B.; Nordlander, P.; Sader, J. E.; Halas, N. J.; Link, S. *Nat. Commun.* **2015,** 6, 7022.
2. Ye, X. C.; Gao, Y. Z.; Chen, J.; Reifsnyder, D. C.; Zheng, C.; Murray, C. B. *Nano Lett.* **2013,** 13, 2163-2171.
3. O'Brien, M. N.; Jones, M. R.; Kohlstedt, K. L.; Schatz, G. C.; Mirkin, C. A. *Nano Lett.* **2015,** 15, 1012-1017.
4. Su, M. -N.; Dongare, P. D.; Chakraborty, D.; Zhang, Y.; Yi, C.; Wen, F.; Chang, W. -S.; Nordlander, P.; Sader, J. E.; Halas, N. J.; Link, S. *Nano Lett.* **2017,** 17, 2575-2583.
5. Yi, C.; Dongare, P. D.; Su, M. -N.; Wang, W.; Chakraborty, D.; Wen, F.; Chang, W. -S.; Sader, J. E.; Nordlander, P.; Halas, N. J.; Link, S. *Proc. Natl. Acad. Sci. U.S.A.* **2017,** 114, 11621-11626.
6. Wang, L.; Nishijima, Y.; Ueno, K.; Misawa, H.; Tamai, N. *J. Phys. Chem. C* **2012,** 116, 17838-17846.
7. Soavi, G.; Tempra, I.; Pantano, M. F.; Cattoni, A.; Collin, S.; Biagioni, P.; Pugno, N. M.; Cerullo, G. *ACS Nano* **2016,** 10, 2251-2258.
8. Kelf, T. A.; Tanaka, Y.; Matsuda, O.; Larsson, E. M.; Sutherland, D. S.; Wright, O. B. *Nano Lett.* **2011,** 11, 3893-3898.
9. Della Picca, F.; Berte, R.; Rahmani, M.; Albella, P.; Bujjamer, J. M.; Poblet, M.; Cortes, E.; Maier, S. A.; Bragas, A. V. *Nano Lett.* **2016,** 16, 1428-1434.
10. Marty, R.; Arbouet, A.; Girard, C.; Mlayah, A.; Paillard, V.; Lin, V. K.; Teo, S. L.; Tripathy, S. *Nano Lett.* **2011,** 11, 3301-3306.